

Uncovering the Hidden Ferroaxial Density Wave as the Origin of the Axial Higgs Mode in RTe₃

Birender Singh^{1*}, Grant McNamara¹, Kyung-Mo Kim¹, Saif Siddique², Stephen D. Funni², Weizhe Zhang³, Xiangpeng Luo³, Piyush Sakrikar¹, Eric M. Kenny¹, Ratnadwip Singha⁴, Sergey Alekseev⁵, Sayed Ali Akbar Ghorashi⁵, Thomas J. Hicken⁶, Christopher Baines⁶, Hubertus Luetkens⁶, Yiping Wang¹, Vincent M. Plisson¹, Michael Geiwitz¹, Connor A. Occhialini⁷, Riccardo Comin⁷, Michael J. Graf¹, Liuyan Zhao³, Jennifer Cano^{5,8}, Rafael M. Fernandes⁹, Judy J. Cha², Leslie M. Schoop⁴ and Kenneth S. Burch¹

¹*Department of Physics, Boston College, Chestnut Hill, MA, USA*

²*Department of Materials Science and Engineering, Cornell University, Ithaca, NY, USA*

³*Department of Physics, University of Michigan, Ann Arbor, MI, USA*

⁴*Department of Chemistry, Princeton University, Princeton, NJ, USA*

⁵*Department of Physics and Astronomy, Stony Brook University, Stony Brook, NY, USA*

⁶*Laboratory for Muon Spin Spectroscopy, Paul Scherrer Institute, CH-5232 Villigen, Switzerland*

⁷*Department of Physics, Massachusetts Institute of Technology, Cambridge, MA, USA*

⁸*Center for Computational Quantum Physics, Flatiron Institute, NY, USA*

⁹*School of Physics and Astronomy, University of Minnesota, Minneapolis, MN, USA*

The recent discovery of an axial amplitude (Higgs) mode in the long-studied charge density wave (CDW) systems GdTe₃ and LaTe₃ suggests a heretofore unidentified hidden order. A theoretical study proposed that the axial Higgs results from a hidden ferroaxial component of the CDW, which could arise from non-trivial orbital texture. Here, we report extensive experimental studies on ErTe₃ and HoTe₃ that possess a high-temperature CDW similar to other RTe₃ (R = rare earth), along with an additional low-temperature CDW with an orthogonal ordering vector. Combining Raman spectroscopy with large-angle convergent beam electron diffraction (LACBED), rotational anisotropy second-harmonic

generation (RA-SHG), and muon-spin relaxation (μ SR), we provide unambiguous evidence that the high-temperature CDW breaks translation, rotation, and all vertical and diagonal mirror symmetries, but not time-reversal or inversion. In contrast, the low-temperature CDW only additionally breaks translation symmetry. Simultaneously, Raman scattering shows the high-temperature CDW produces an axial Higgs mode while the low-temperature mode is scalar. The weak monoclinic structural distortion and clear axial response in Raman and SHG are consistent with a ferroaxial phase in RTe₃ driven by coupled orbital and charge orders. Thus, our study provides a new standard for uncovering unconventional orders and confirms the power of Higgs modes to reveal them.

In most cases, the symmetries broken by a centrosymmetric CDW state with a single- q are entirely encoded in the wave vector \vec{q}_{CDW} . The magnitude of \vec{q}_{CDW} gives the inverse period, reflecting the translational symmetry breaking. The orientation of \vec{q}_{CDW} with respect to the atomic wavevectors may break point symmetries, such as rotational and mirror symmetries. Recently, attention has turned to unconventional CDW that break additional symmetries other than those encoded by \vec{q}_{CDW} due to the simultaneous condensation of secondary ferroic order parameters^{1–12}. Identifying and understanding such systems is challenging, requiring uncovering which material properties are reflected in the order parameter. Beyond probe limitations, certain broken symmetries are often hidden due to the absence of a clear conjugate field to which they couple.

These unconventional CDW orders could be observed and understood through their novel quasi-particles with properties inherited from the orders in which they emerge^{13–15}. Indeed, a new phase's fundamental broken symmetries (or topologies) should be reflected in their collective excitations' properties^{16–19}. Consider, for example, a conventional CDW described by a Ginzburg-Landau approach with an order parameter ($\psi = \eta e^{i\phi}$), where η reflects the distortion amplitude and ϕ the phase with respect to the lattice. The resulting free energy of the ordered state (Fig. 1a) produces two new low-energy excitations of the order parameter field (amplitudon (Higgs), and phason (Goldstone))¹³. Since $\psi \neq 0$ typically breaks symmetries

determined by \vec{q}_{CDW} , the amplitude mode ($|\psi|^2$) transforms trivially under the crystal symmetry²⁰. This is in sharp contrast with a multi-component CDW described by two order parameters ψ_1 and ψ_2 that transform differently under the crystal symmetries but share the same \vec{q}_{CDW} . Now, the collective Higgs mode ($\psi_1\psi_2^* + \psi_1^*\psi_2$) will generally transform non-trivially under the symmetries of the crystal²¹.

One example is the A_2 mode seen in the Raman response of URu_2Si_2 ²², which was proposed to result from a previously hidden orbital ferroaxial state²³. Such states are rare and unlike other ferroic orders (Fig. 1b). It is described as a circulating pattern of electric dipoles whose order parameter, an axial vector, preserves both spatial inversion and time reversal symmetries, and hence, does not couple linearly to electric and magnetic fields^{24–26}. As such, the observation of an axial Higgs mode in $GdTe_3$ and $LaTe_3$ ²⁷ was quite surprising as it indicated a hidden order whose specific type of ferroic density wave (Fig. 1b) and thus origin have yet to be uncovered. Indeed, unlike other materials where unconventional density waves are believed to exist, the entire rare-earth tritellurides (RTe_3) have weak electron-electron correlations, no lattice frustration (e.g., as in Kagome systems), and in some cases, no f -electron or magnetic moments. Thus, the CDW in RTe_3 had been considered conventional, possessing one or two unidirectional, incommensurate charge orders that only break some rotation and mirror symmetries related to the direction of \vec{q}_{CDW} ^{9,28–33} (Fig. 1c). Interestingly, recent theoretical³⁴ and experimental studies³⁵ suggested the axial Higgs mode could emerge from a multi-component CDW involving orbital and charge order. In particular, the condensation of two CDW order parameters with different orbital compositions gave rise to a ferroaxial order³⁴.

Beyond the type of unconventional CDWs, the universality of the axial Higgs across the RTe_3 series is unclear. As shown in Fig. 1f, rare-earth elements heavier than Gd can reduce T_{CDW1} by half and produce a second subdominant CDW order below a lower temperature (T_{CDW2})^{9,36}. Thus, for this study we turned to the heavier elements, which also provide a built-in control experiment wherein the broken symmetries of the system and Higgs modes emerging from different CDWs are measured in the same compound. Raman

scattering reveals that the high-temperature order breaks all vertical and diagonal mirrors, producing an axial Higgs across the series. Consistent with a ferroaxial order emerging from orbital texture, electron diffraction confirms that the lattice mirror breaking is extremely weak. At the same time, the electron diffraction and rotational-anisotropy second-harmonic generation (RA-SHG) show the two-fold (C_{2z})-rotation and inversion symmetries are preserved. Muon spin relaxation demonstrates the CDW state does not break time reversal. Within the same experiments on the same sample, we find that the low-temperature CDW only breaks an additional translational symmetry with respect to the high-temperature CDW phase, producing a scalar Higgs mode. Thus, the experimentally observed broken symmetries (Fig. 1d) prove the axial Higgs mode results from an unconventional ferroaxial CDW. In addition, they provide compelling evidence of an electronic ferroaxial CDW emerging from a combined orbital and charge order.

Amplitude modes of RTe₃

RTe₃ features two tetragonal Te-RTe-Te slabs separated by van-der-Waals gaps along the c -axis, Fig. 1e, enabling exfoliation^{37,38}. The p -orbitals of the Te square-net make up the Fermi surface with p_x (p_y) parallel to the a' , 45° to a -axis (b' , 45° to b -axis) axis. The glide-plane along b -axis, between the Te-sheets (Fig. 1e), produces slightly non-equivalent in-plane lattice parameters, resulting in a formally orthorhombic space group^{9,36}, but is weak enough that the normal state is effectively tetragonal^{39,40}. The CDW order has the wave-vector $\vec{q}_{CDW} = (2/7)b^*$ whose direction is selected by this effective glide field (Fig. 1c)^{9,36,41}. Within the conventional scenario, as shown in Fig. 1c, the unidirectional CDW order breaks translation, C_4 -rotation and mirrors $m_{a'}$ (pink, 45° to m_a) and $m_{b'}$ (blue, 45° to m_b). However, for the ferroaxial CDW scenario, all mirrors parallel to the ferroaxial axis are broken, namely the vertical mirrors m_a (red) and m_b (green), as well as the diagonal mirrors $m_{a'}$ and $m_{b'}$ (Fig. 1d). This order is unconventional, breaking symmetries beyond those of \vec{q}_{CDW} . Consequently, the system goes directly from a quasi-tetragonal to a monoclinic phase.

To simultaneously investigate the lattice and CDW symmetries, we carefully measured the polarization- and temperature-dependent Raman scattering in ErTe_3 . Figure 2a shows the Raman spectra from the crystalline a - b plane at 290 K (i.e., in the normal state $T > T_{CDW1} \approx 265\text{K}$), 190 K ($T_{CDW1} > T > T_{CDW2} \approx 155\text{K}$), and 10 K ($T < T_{CDW2}$) with the incident and scattered light polarized parallel to the a -axis (i.e., in the parallel (XX) configuration). In the normal phase ($T > T_{CDW1}$), four phonon modes are seen whose symmetries, discussed later, are consistent with a tetragonal, completely undistorted lattice. Upon entering the CDW1 phase, new modes appear either from the zone-folding by the CDW1 or due to the CDW Higgs mode^{27,38}. Upon further cooling below the second CDW transition temperature, additional weak modes at low energy are observed, suggesting further translation symmetry breaking (see the 10 K spectra in Fig. 2a).

The temperature evolution of most modes measured via the crossed-circular polarization Raman response ($\sigma^+ \sigma^-$) is shown in Fig. 2b. This and the other polarization channels (Supplementary Section 1) are consistent with previous measurements^{27,38,42}. As expected from zone-folded phonons, all but two modes appearing below T_{CDW1} are nearly temperature-independent. In contrast, the substantial energy shift of the 4.1 meV and 8.8 meV modes and their vanishing near T_{CDW2} and T_{CDW1} , respectively, is consistent with the assignment of these excitations to the amplitude modes of the respective CDW orders^{10,33}. As shown in Fig. 2c, the CDW2 amplitude mode (4.1 meV) is well described within a mean-field theory¹³, while the high-temperature CDW1 Higgs mode requires a two-mode interaction model^{10,38} to account for the avoided crossing at ~ 130 K with the phonon at ~ 7.5 meV (Supplementary Section 1). The coupling of CDW1 amplitude mode with the folded phonon (7.5 meV) reflects their identical symmetry.

Vertical and diagonal mirror symmetry breaking

We turned to angle-resolved Raman measurements to determine the symmetry of the high- and low-temperature CDW orders and their Higgs modes. It is helpful first to consider the vertical and diagonal

mirrors of the Te square-net, shown in Fig. 3a,b as red (m_a) and pink ($m_{a'}$) lines. As shown in Fig. 1c, since the \vec{q}_{CDW} is along b -axis, in a conventional scenario the CDW would break the mirrors $m_{a'}$ and $m_{b'}$, but not those normal or parallel to it (i.e., m_a and m_b). However, in the proposed case of unconventional CDW we anticipate all vertical and diagonal mirrors to be broken. To see how this affects the Raman response, consider that in RTe₃ at our excitation energy, we excite from primarily the Te p_z orbitals such that an a' (b') polarization selects a transition to p_x (p_y). Hence, in the parallel polarization configuration, the Raman transitions occur between the same orbitals and, as such, are sensitive to $m_{a',b'}$ mirrors that leave the orbitals unchanged. However, since crossed polarization configuration requires Raman transitions between orbitals, these are more sensitive to the $m_{a,b}$ mirrors.

Thus, we first evaluate the parallel polarization configuration in Fig. 3a, with an initial incident (\vec{E}_i , solid green arrow) and outgoing (\vec{E}_o , solid dark yellow arrow) electric fields along the a -direction (i.e., aa (XX 90°) configuration). The mirror m_a takes the aa configuration to itself (dashed vertical arrows \vec{E}'_o and \vec{E}'_i), whereas mirror $m_{a'}$ takes the aa to bb (YY 0°) configuration, horizontal arrows, \vec{E}'_o and \vec{E}'_i . The mirror behaves distinctly in the crossed polarization configuration, shown in Fig. 3b. For example, for \vec{E}_i along the a' and \vec{E}_o along b' (i.e., $a'b'$ configuration), m_a swaps the $a'b'$ to $b'a'$ configuration, while under mirror $m_{a'}$ they remain unchanged. Within this scenario, for the perfect square-net, one would expect equal Raman intensity under the m_a and $m_{a'}$ mirror operations (similarly for m_b (green) and $m_{b'}$ (blue)). Noting that in the orthorhombic phase from the conventional CDW, the $m_{a'}$ ($m_{b'}$) mirror is broken, we expect distinct Raman responses for the aa and bb configurations. However, since m_a (m_b) maps aa (bb) onto itself, the angular response in parallel polarization can produce a two-fold angular response (or two inequivalent two-fold responses along aa and bb). In the crossed polarization, a four-fold angular response is expected, as preservation of the m_a and m_b mirrors forces the $a'b'$ and $b'a'$ response to be identical.

Armed with this intuition, we note a tetragonal (D_{4h} point group) symmetry will produce phonon

modes with A_{1g} and B_{1g} symmetry in our scattering geometry. Figure 3c,d shows the angular dependence of the intensity of the 8.1 meV phonon modes in the undistorted phase at 290 K. We observed angle independent intensity of the 8.1 meV in the parallel polarization configuration, Fig. 3c, and no signal in the crossed-polarization (Fig. 3d). This mode and those at 14.5 meV and 16.2 meV are well fit by the response expected of A_{1g} symmetry (solid line in Fig. 3c) and thus labeled $A_{1g}^{(1,2,3)}$ respectively (superscript distinguishes the modes by energy). We also observed a phonon mode with B_{1g} symmetry at 11.0 meV (see Supplementary Section 2). This is consistent with previous works^{33,43} and the normal phase having a tetragonal, D_{4h} symmetry with all vertical (m_a, m_b) and diagonal ($m_{a'}, m_{b'}$) mirrors, as shown by solid lines in Fig. 3a,b, along with in-plane horizontal mirror and C_4 -rotation. In the CDW1 phase (190 K), the phonon mode at 11.3 meV reveals unequal response along aa and bb parallel polarization configuration (Fig. 3e), confirming broken mirrors $m_{a'}$ and $m_{b'}$ (shown with dashed lines). However, the four-fold response in cross-polarization (Fig. 3f) suggests m_a and m_b remain (solid lines). Indeed, the observed angular response of this and another B_g mode are well fit with the respective Raman tensors of the D_{2h} point group (see Supplementary Section 2). Notably, no change in the angular response of these phonon modes is observed below $T < T_{CDW2}$ (see Fig. 3e,f, dark blue), reflecting no additional symmetry breaking (except translation) due to the second CDW order.

Distinct from the response of all other modes, the CDW1 amplitude mode (Fig. 3g,h) and the folded phonon mode at 7.5 meV (Fig. 3i,j) reveal a two-fold angular response in the parallel and, surprisingly, the crossed configurations. A similar symmetry of the two modes is expected as they mix and reveal an avoided crossing. Nonetheless, their anomalous response is identical to the axial Higgs mode in LaTe₃ and GdTe₃ (well fit with the antisymmetric Raman tensor $R_{CDW} = \begin{pmatrix} a & d \\ -d & b \end{pmatrix}$). The two-fold angular response in parallel polarization reflects the unidirectional nature of the CDW order with the charge fluctuations along the a -axis (wave-vector along the b -axis)³³ and is consistent with the breaking of the $m_{a'}$ and $m_{b'}$ mirrors. However,

more uncommon is the response in the crossed-polarization configuration (Fig. 3h), which is also two-fold along the a' -direction reflecting the broken m_a and m_b mirror symmetries; consistent with a monoclinic rather than orthorhombic state. Since the folded phonon has the same response, we conclude that monoclinic symmetry exists in the electronic and lattice sectors.

Next, we explore the symmetry of low-temperature CDW2 amplitude mode, where we expect a trivial angular response, as all vertical and diagonal mirror symmetries, as well as the C_4 rotational symmetry, are already broken. As shown in Fig. 3k,l, we find CDW2 amplitude mode exhibits a four-fold angular response in both parallel and crossed-polarization configurations, similar to the symmetric A_g phonon mode (Fig. 3e,f). Thus, the CDW2 amplitude mode possesses a scalar representation, reflecting that the low-temperature order only breaks the additional translation symmetry without further lowering the point group. Moreover, the simultaneous detection of the axial (two-fold) high-temperature CDW1 and the scalar low-temperature CDW2 amplitude modes within the system rule out resonant or other Raman artifacts as the origin of the two-fold anisotropic CDW1 amplitude mode response. These findings are further confirmed by additional measurements performed on HoTe₃ as well as ErTe₃ measured both at Boston College (BC) and Massachusetts Institute of Technology (MIT) (see Supplementary Section 2).

To look for lattice changes more directly, we employed *in-situ* cryogenic scanning transmission electron microscopy (STEM). As shown in Fig. 4b, the CDW1 transition was observed directly via the emergence of satellite peaks in the selected area electron diffraction (SAED). However, atomic-resolution STEM imaging using a high-angle annular dark-field detector (HAADF) at 120 K (Figs. 4c,d) did not show the monoclinic distortion from the CDW transitions. This suggests that the monoclinic distortion seen with Raman scattering might be quite small. Thus, we turned to large-angle convergent beam electron diffraction (LACBED), which enhances the symmetry information encoded in conventional CBED patterns⁴⁴ by extending the angular range of information in the reciprocal space by defocus (see Supplementary Section 4)^{45,46}. Since a crystal's

structure governs how electrons are scattered, the symmetries of the crystal are reflected in the diffraction pattern⁴⁷, via variations in features such as lines, fringes, and intensity captured within LACBED. Figures 4f-h show the central disk of LACBED patterns from an ErTe_3 flake (shown in Fig. 4a) aligned along the [001] zone-axis at 300 K ($T > T_{CDW1}$), 240 K ($T_{CDW1} > T > T_{CDW2}$), and 120 K ($T < T_{CDW2}$), respectively. Key features are highlighted by white dashed lines, with the LACBED pattern at 300 K exhibiting a four-fold rotational symmetry. In addition, the image is symmetric when two sets of mirror planes perpendicular to the $\langle 100 \rangle$ (m_a, m_b) and $\langle 110 \rangle$ axes ($m_{a'}, m_{b'}$) are applied. These results are identical to the simulated LACBED pattern shown in Fig. 4e for tetragonal symmetry. Upon cooling below the CDW1 transition (Fig. 4g), in the right half of the LACBED pattern, the dark fringes smear out (overlaid dashed lines) while a noticeable enhancement in the intensity is observed. These changes in the LACBED pattern reflect the CDW1 order breaking of the mirror $m_a, m_b, m_{a'}$, and $m_{b'}$ symmetries. No further symmetry change in the LACBED pattern is noticed with cooling below T_{CDW2} , at 120 K (Fig. 4h). Supplementary Section 4 quantifies the symmetries in the LACBED patterns.

Spatial inversion and time-reversal symmetries

The experimental findings presented using Raman scattering and LACBED suggest the high-temperature CDW1 order is ferroaxial. However, these techniques do not probe the crucial spatial inversion and time-reversal symmetries needed to exclude other ferroic order parameters (e.g., polar or magnetic). Thus, we turned to RA-SHG, which detects broken inversion through electric dipole contributions and broken mirror symmetries in centrosymmetric phases through the electric quadrupole (EQ)^{48,49}. Consistent with the absence of inversion symmetry breaking and the presence of out-of-plane C_{2z} -rotational symmetry, no SHG signal was observed in bulk ErTe_3 and LaTe_3 crystals near normal incidence. In ErTe_3 , the RA-SHG was too weak at any temperature to clearly distinguish the symmetry breaking due to the CDW. Thus, we focused on RA-SHG in LaTe_3 where a clear signal was resolved at an 11.5 angle of incidence from 80 K

to 290 K, well below the CDW ordering temperature ($T_{\text{CDW}} \approx 670$ K). The RA-SHG polar plots in the four polarization channels at 80 K are shown in Fig. 5a-d. Consistent with the Raman data, the broken mirror symmetries are directly reflected in the polarization dependent SHG response. Specifically, in the $P_{\text{in}}P_{\text{out}}$ configuration (Fig. 5a), the response is not symmetric about the m_a and m_b mirrors, showing they are broken. More crucially, the responses of the three other polarization configurations, $P_{\text{in}}S_{\text{out}}$, $S_{\text{in}}P_{\text{out}}$, $S_{\text{in}}S_{\text{out}}$, do not respect any of the vertical and diagonal mirrors, showing the system is indeed monoclinic. Nonetheless, all four channels reveal a two-fold rotational symmetry, showing the highest possible symmetry point group for the CDW state is C_{2h} . Indeed, the EQ contribution to the SHG under C_{2h} fits well with the experimental data, as shown by the orange lines in Fig. 5a-d (Supplementary Section 5). Surveying fourteen locations across the sample and at other temperatures reveals results consistent with those in Fig. 5a-d. Hence, the RA-SHG indicates the CDW state is centrosymmetric, requiring ferroaxial CDW order (Fig. 1b).

To determine if the order breaks time-reversal symmetry, we employed muon spin relaxation (μSR), a sensitive probe of local magnetic fields⁵⁰. Here, spin-polarized positive muons are implanted in the sample, and the time evolution of the μ -spin polarization in the local magnetic field is measured via the preferential emission of a positron in the μ -spin direction upon decay. The μSR from ErTe_3 showed large fluctuating Er^{3+} moment above 200 K, which do not exhibit long-range magnetic order, masking potential small contributions from orbital moments. Thus, we focus on the zero-field (ZF) μSR results from LaTe_3 below T_{CDW} , shown in Fig. 5e. The lack of observable oscillations combined with the weak depolarization indicates the absence of long-range magnetic order. We fit the time-dependent curves with the Gaussian Kubo-Toyabe (GKT) function, which describes depolarization via densely packed, randomly oriented moments⁵¹ (Fig. 5e, see Supplementary Section 6). We can unambiguously rule out an increase in relaxation rate (σ) at low temperatures, the typical signature of time-reversal symmetry breaking (TRSB). If anything, there could be a slight decrease in σ at low temperatures, which one may speculate is related to a change in muon-stopping

site populations. Our stopping site calculations, see Supplementary Section 6, suggest that the observed relaxation is consistent with depolarisation due to the nuclear moments of ^{139}La . Based on these results, any ordering of novel electronic moments would produce a local field that must be less than the nuclear magnetic fields and is unlikely to be a source of TRSB. Finally, as discussed in Supplementary Section 3, the absence of TRSB is further supported by our helicity-resolved Raman response and the equivalent Stokes (S) and anti-Stokes (aS) Raman susceptibilities^{52–57}.

Discussion

Our extensive results demonstrate that the unconventional CDW1 in the entire RTe_3 family breaks all vertical and diagonal mirrors but not inversion, C_{2z} -rotation, or time-reversal symmetries. Thus, the CDW involves a spontaneous breaking of multiple, distinct symmetries. Specifically, the CDW includes an out-of-plane ferroaxial moment that transforms as A_{2g} in D_{4h} (Fig. 1a), lowering the system to C_{4h} . However, this combines with the uniaxial character of the CDW modulation, which transforms as B_g in C_{4h} , further lowering the point group to C_{2h} . Thus, the axial Higgs mode results from an unconventional ferroic CDW transition, requiring the multi-component condensation of the CDW order parameters transforming as two different irreducible representations. Indeed, a conventional, single-component CDW could not lead to the emergence of a ferroaxial moment as it only breaks the symmetries associated with the single \vec{q}_{CDW} . This assertion is further corroborated by the amplitude mode of the low-temperature CDW having a scalar representation (A_g). Indeed, the second low-temperature CDW is conventional, only involving the further breaking of translation symmetry of the high-temperature phase. Furthermore, the Raman scattering only reveals one phonon that directly manifests the monoclinic distortion. The modeling of the angular Raman response of the distinct single- and multi-domain ferroaxial state is discussed in Supplementary section 2. Thus, the Raman and STEM measurements reveal the CDW produces a nearly orthorhombic lattice distortion. However, the clear axial property of the amplitude mode and monoclinic space group seen in SHG suggests that the ferroaxial

order has a much stronger imprint on the electronic sector. These results strongly suggest the ferroaxial component of the CDW results from an additional electronic component.

These findings align with a recent theoretical description emphasizing the role of both orbital and charge order in the RTe_3 CDW³⁴ that also appears to be substantiated by an STM study of CeSbTe ³⁵. Specifically, four of us revisited the microscopic model outlined in Ref. ³¹, where it was assumed that since \vec{q}_{CDW} is along the Te square-net diagonal, the modulation of the occupation of the p_x and p_y orbitals was in phase. However, the Ginzburg–Landau model can be generalized to allow for a different CDW order parameter on the weakly hybridized p_x and p_y orbitals. Namely, within this microscopic model, the charge order pattern consists of two coexisting order parameters with the same \vec{q}_{CDW} , but distinct in either phase or amplitude. For negligible electron-phonon coupling, the model predicts a polar component in the CDW state (i.e., breaks inversion symmetry). However, the secondary order can become ferroaxial once the electron-phonon coupling is accounted for. If this ferroaxial CDW is realized, the extent to which this orbital-driven order is reflected in the electronic structure and its implications for quantum geometry remain open questions. Nonetheless, our experimental observations establish that a previously hidden multi-component unconventional ferroaxial CDW order and associated axial Higgs mode exists across the RTe_3 series. As such, these systems may constitute a new class of density wave systems where unconventional order emerges purely from a strong coupling of the lattice, charge, and orbital degrees of freedom. These results further suggest measuring the properties of the Higgs modes in other CDW systems, such as dichalcogenides (TiSe_2) and kagome metals (CsV_3Sb_5), would provide important insights into their novel ground states.

References

1. Fradkin, E., Kivelson, S. A. & Tranquada, J. M. Colloquium: Theory of intertwined orders in high temperature superconductors. *Rev. Mod. Phys.* **87**, 457 (2015).
2. Comin, R. *et al.* Symmetry of charge order in cuprates. *Nature Materials* **14**, 796–800 (2015). URL <https://doi.org/10.1038/nmat4295>.
3. Tam, C. C. *et al.* Charge density waves in infinite-layer NdNiO_2 nickelates. *Nature Materials* **21**, 1116–1120 (2022).
4. Liu, G. *et al.* Electrical switching of ferro-rotational order in nanometre-thick 1T-TaS₂ crystals. *Nat. Nanotechnol.* **18**, 854–860 (2023). URL <https://doi.org/10.1038/s41565-023-01403-5>.
5. Luo, X. *et al.* Ultrafast modulations and detection of a ferro-rotational charge density wave using time-resolved electric quadrupole second harmonic generation. *Phys. Rev. Lett.* **127**, 126401 (2021).
6. Xu, S.-Y. *et al.* Spontaneous gyrotropic electronic order in a transition-metal dichalcogenide. *Nature* **578**, 545–549 (2020). URL <https://doi.org/10.1038/s41586-020-2011-8>.
7. Hart, J. L. *et al.* In operando cryo-stem of pulse-induced charge density wave switching in TaS₂. *Nature Communications* **14** (2023). URL <https://doi.org/10.1038/s41467-023-44093-2>.
8. Xi, X. *et al.* Strongly enhanced charge-density-wave order in monolayer NbSe₂. *Nature Nanotechnology* **10**, 765–769 (2015). URL <http://dx.doi.org/10.1038/nnano.2015.143>.
9. Yumigeta, K. *et al.* Advances in rare-earth tritelluride quantum materials: Structure, properties, and synthesis. *Adv. Sci.* **8**, 2004762 (2021).

10. Lavagnini, M. *et al.* Raman scattering evidence for a cascade evolution of the charge-density-wave collective amplitude mode. *Physical Review B* **81**, 081101(R) (2010). URL <https://link.aps.org/doi/10.1103/PhysRevB.81.081101>.
11. Kwon, S. *et al.* Dual higgs modes entangled into a soliton lattice in CuTe. *Nature Communications* **15**, 984 (2024).
12. Hildebrand, B. *et al.* Local real-space view of the achiral 1T-TiSe₂ 2×2×2 charge density wave. *Phys. Rev. Lett.* **120**, 136404 (2018). URL <https://link.aps.org/doi/10.1103/PhysRevLett.120.136404>.
13. Grüner, G. *Density Waves in Solids* (Addison-Wesley, Reading, MA, 1994).
14. Matsunaga, R. *et al.* Higgs amplitude mode in the BCS superconductors Nb_{1-x}Ti_xN induced by terahertz pulse excitation. *Phys. Rev. Lett.* **111**, 057002 (2013). URL <https://doi.org/10.1103/PhysRevLett.111.057002>.
15. Xie, Y.-M. & Nagaosa, N. Phase shifts, band geometry and responses in triple-Q charge and spin density waves (2024). URL <https://arxiv.org/abs/2405.00292>. [2405.00292](https://arxiv.org/abs/2405.00292).
16. Souliou, S.-M. *et al.* Raman scattering from higgs mode oscillations in the two-dimensional antiferromagnet Ca₂RuO₄. *Physical Review Letters* **119**, 067201 (2017). URL <https://doi.org/10.1103/PhysRevLett.119.067201>.
17. Schwarz, L. *et al.* Classification and characterization of nonequilibrium higgs modes in unconventional superconductors. *Nature Communications* **11**, 287 (2020). URL <https://doi.org/10.1038/s41467-019-13763-5>.

18. Puviani, M. *et al.* Calculation of an enhanced A_{1g} symmetry mode induced by higgs oscillations in the raman spectrum of high-temperature cuprate superconductors. *Physical Review Letters* **127**, 197001 (2021).
19. Wulferding, D. *et al.* Collective magnetic higgs excitation in a pyrochlore ruthenate. *npj Quantum Materials* **8**, 40 (2023).
20. Pekker, D. & Varma, C. M. Amplitude/higgs modes in condensed matter physics. *Annual Review of Condensed Matter Physics* **6**, 269–297 (2015).
21. Fernandes, R. M., Orth, P. P. & Schmalian, J. Intertwined vestigial order in quantum materials: Nematicity and beyond. *Annu. Rev. Condens. Matter Phys.* **10**, 133–154 (2019). URL <https://doi.org/10.1146/annurev-conmatphys-031218-013200>.
22. Kung, H.-H. *et al.* Chirality density wave of the "hidden order" phase in URu_2Si_2 . *Science* **347**, 1339–1342 (2015). URL <https://doi.org/10.1126/science.1259729>.
23. Hlinka, J., Privratska, J., Ondrejkovic, P. & Janovec, V. Symmetry guide to ferroaxial transitions. *Phys. Rev. Lett.* **116**, 177602 (2016).
24. Van Aken, B. B., Rivera, J.-P., Schmid, H. & Fiebig, M. Observation of ferrotoroidic domains. *Nature* **449**, 702–705 (2007).
25. Hayashida, T. *et al.* Visualization of ferroaxial domains in an order-disorder type ferroaxial crystal. *Nature Communications* **11**, 4582 (2020).
26. Day-Roberts, E., Fernandes, R. M. & Birol, T. Piezoresistivity as an order parameter for ferroaxial transitions (2024). URL <https://arxiv.org/abs/2405.02149>.
27. Wang, Y. *et al.* Axial higgs mode detected by quantum pathway interference in RTe_3 . *Nature* **606**, 896–901 (2022). URL <https://doi.org/10.1038/s41586-022-04746-6>.

28. Fang, A., Ru, N., Fisher, I. R. & Kapitulnik, A. STM studies of TbTe_3 : Evidence for a fully incommensurate charge density wave. *Phys. Rev. Lett.* **99**, 046401 (2007). URL <https://doi.org/10.1103/PhysRevLett.99.046401>.

29. Moore, R. G. *et al.* Fermi surface evolution across multiple charge density wave transitions in ErTe_3 . *Phys. Rev. B* **81**, 073102 (2010). URL <https://doi.org/10.1103/PhysRevB.81.073102>.

30. Chen, R. Y., Hu, B. F., Dong, T. & Wang, N. L. Revealing multiple charge-density-wave orders in TbTe_3 by optical conductivity and ultrafast pump-probe experiments. *Phys. Rev. B* **89**, 075114 (2014). URL <https://doi.org/10.1103/PhysRevB.89.075114>.

31. Yao, H., Robertson, J. A., Kim, E.-A. & Kivelson, S. A. Theory of stripes in quasi-two-dimensional rare-earth tellurides. *Phys. Rev. B* **74**, 245126 (2006).

32. Johannes, M. D. & Mazin, I. I. Fermi surface nesting and the origin of charge density waves in metals. *Phys. Rev. B* **77**, 165135 (2008).

33. Eiter, H.-M. *et al.* Alternative route to charge density wave formation in multiband systems. *Proc. Natl. Acad. Sci. USA* **110**, 64–69 (2013). URL <https://doi.org/10.1073/pnas.1214745110>.

34. Alekseev, S., Ghorashi, S. A. A., Fernandes, R. M. & Cano, J. Charge density waves with nontrivial orbital textures in rare earth tritellurides. *Phys. Rev. B* **110**, 205103 (2024). URL <https://doi.org/10.1103/PhysRevB.110.205103>.

35. Que, X. *et al.* Visualizing \$p\$-orbital texture in the charge-density-wave state of CeSbTe . *arXiv* (2024). [2408.07351](https://arxiv.org/abs/2408.07351).

36. Ru, N. *et al.* Effect of chemical pressure on the charge density wave transition in rare-earth tritellurides RTe_3 . *Physical Review B* **77**, 035114 (2008). URL <https://doi.org/10.1103/PhysRevB.77.035114>.

37. Lei, S. *et al.* High mobility in a van der waals layered antiferromagnetic metal. *Science Advances* **6** (2020).

38. Chen, Y. *et al.* Raman spectra and dimensional effect on the charge density wave transition in GdTe₃. *Applied Physics Letters* **115**, 151905 (2019). URL <https://doi.org/10.1063/1.5118870>.

39. Singh, A. G. *et al.* Emergent tetragonality in a fundamentally orthorhombic material. *Science Advances* **10** (2024). URL <https://www.science.org/doi/10.1126/sciadv.adk3321>.

40. Kivelson, S. A., Pandey, A., Singh, A. G., Kapitulnik, A. & Fisher, I. R. Emergent z2 symmetry near a charge density wave multicritical point. *Physical Review B* **108**, 205141 (2023). URL <https://doi.org/10.1103/PhysRevB.108.205141>.

41. Straquadine, J. A. W., Ikeda, M. S. & Fisher, I. R. Evidence for realignment of the charge density wave state in ErTe₃ and TmTe₃ under uniaxial stress via elastocaloric and elastoresistivity measurements. *Phys. Rev. X* **12**, 021046 (2022). URL <https://doi.org/10.1103/PhysRevX.12.021046>.

42. Maschek, M. *et al.* Competing soft phonon modes at the charge-density-wave transitions in DyTe₃. *Phys. Rev. B* **98**, 094304 (2018).

43. Lazarević, N., Popović, Z. V., Hu, R. & Petrović, C. Evidence of coupling between phonons and charge-density waves in ErTe₃. *Phys. Rev. B* **83**, 024302 (2011).

44. Zuo, J. M. & Spence, J. C. H. *Electron Microdiffraction* (Springer Science & Business Media, 2013).

45. Tanaka, M., Saito, R., Ueno, K. & Harada, Y. Large-Angle Convergent-Beam Electron Diffraction. *Journal of Electron Microscopy* **29**, 408–412 (1980). URL <https://doi.org/10.1093/oxfordjournals.jmicro.a050262>. <https://academic.oup.com/jmicro/article-pdf/29/4/408/2622046/29-4-408.pdf>.

46. Morniroli, J.-P. *Large-Angle Convergent-Beam Electron Diffraction Applications to Crystal Defects* (CRC Press, Boca Raton, 2002), 1st edn.

47. Buxton, B. F., Eades, J. A., Steeds, J. W. & Rackham, G. M. The symmetry of electron diffraction zone axis patterns. *Philosophical Transactions of the Royal Society A: Mathematical, Physical and Engineering Sciences* **281**, 171–194 (1976). URL <https://doi.org/10.1098/rsta.1976.0024>.

48. Jin, W. *et al.* Observation of a ferro-rotational order coupled with second-order nonlinear optical fields. *Nat. Phys.* **16**, 42–46 (2020). URL <https://doi.org/10.1038/s41567-019-0695-1>.

49. Ahn, Y. *et al.* Electric quadrupole second-harmonic generation revealing dual magnetic orders in a magnetic weyl semimetal. *Nature Photonics* **18**, 26–31 (2024). URL <https://doi.org/10.1038/s41566-023-01300-2>.

50. Yaouanc, A. A. & de Reotier, P. D. *Muon Spin Rotation, Relaxation, and Resonance: Applications to Condensed Matter* (Oxford University Press, 2011).

51. Kubo, R. & Toyabe, T. *Magnetic Resonance and Relaxation* (North Holland, 1967).

52. Zhang, Y. *et al.* Magnetic order-induced polarization anomaly of raman scattering in 2D magnet CrI₃. *Nano Lett.* **20**, 729–734 (2020).

53. Jin, W. *et al.* Tunable layered-magnetism-assisted magneto-raman effect in a two-dimensional magnet CrI₃. *Proc. Natl. Acad. Sci. USA* **117**, 24664–24669 (2020). URL <https://www.pnas.org/cgi/doi/10.1073/pnas.2012980117>.

54. Huang, B. *et al.* Tuning inelastic light scattering via symmetry control in the two-dimensional magnet CrI₃. *Nature Nanotechnology* **15**, 212–216 (2020). URL <https://doi.org/10.1038/s41565-019-0598-4>.

55. Cenker, J. *et al.* Direct observation of two-dimensional magnons in atomically thin CrI₃. *Nature Physics* **17**, 20–25 (2021). URL <https://doi.org/10.1038/s41567-020-0999-1>.

56. Loudon, R. Time-reversal symmetry in light-scattering theory. *Journal of Raman Spectroscopy* **7**, 10–14 (1978). URL <https://doi.org/10.1002/jrs.1250070107>.

57. Wang, Y. *et al.* The range of non-kitaev terms and fractional particles in α -RuCl₃. *npj Quantum Materials* **5**, 1–8 (2020). URL <https://doi.org/10.1038/s41535-020-0216-6>.

58. Gray, M. J. *et al.* A cleanroom in a glovebox. *Rev. Sci. Instrum.* **91**, 073909 (2020). URL <https://doi.org/10.1063/5.0006462>.

59. Tian, Y. *et al.* Low vibration high numerical aperture automated variable temperature Raman microscope. *Review of Scientific Instruments* **87**, 043105 (2016).

60. Goodge, B. H., Bianco, E., Schnitzer, N., Zandbergen, H. W. & Kourkoutis, L. F. Atomic-resolution cryo-stem across continuously variable temperatures. *Microscopy and Microanalysis* **26**, 439–446 (2020). URL <https://doi.org/10.1017/S1431927620001427>.

61. Amato, A. *et al.* The new versatile general purpose surface-muon instrument (gps) based on silicon photomultipliers for μ sr measurements on a continuous-wave beam. *Review of Scientific Instruments* **88** (2017).

62. Suter, A. & Wojek, B. Musrfit: a free platform-independent framework for μ sr data analysis. *Physics Procedia* **30**, 69–73 (2012).

63. Hayami, S., Yatsushiro, M., Yanagi, Y. & Kusunose, H. Classification of atomic-scale multipoles under crystallographic point groups and application to linear response tensors. *Phys. Rev. B* **98**, 165110 (2018). URL <https://link.aps.org/doi/10.1103/PhysRevB.98.165110>.

Methods

Crystal growth High-quality ErTe_3 single crystals were grown in an excess of tellurium (Te) via a self-flux technique. Te (metal basis > 99.999% Sigma-Aldrich) was first purified to remove oxygen contamination and then mixed with rare earth (> 99.9%, Sigma-Aldrich) in a ratio of 97:3. The mixture was sealed in an evacuated quartz ampoule and heated to 900 °C over a period of 12 h and then slowly cooled down to 550 °C at a rate of 2 °C h⁻¹. The crystals were separated from the flux via centrifugation at 550 °C.

Sample preparation and vacuum transfer Rare-earth tritellurides (RTe_3) are easily oxidized upon exposure. Thus it is crucial to keep these materials under an inert environment to prevent their oxidation. In our study, we have used freshly exfoliated samples for all the measurements. The samples were exfoliated onto SiO_2/Si substrates and characterized using unpolarized Raman spectroscopy within an argon-filled glovebox. Then, the exfoliated samples were transferred directly to a low-temperature cryostat under high vacuum (1.0 $\times 10^{-7}$ mbar) using a transfer suitcase⁵⁸. As described previously,^{27,37} this ensures the crystal orientation, atomically flat surfaces free from contamination and oxidation, as confirmed by TEM, and in Raman via the absence of Te oxide peaks and the polarization dependence.

Raman Scattering The Raman measurements were performed with a custom-built low-temperature Raman set up in the backscattering configuration. The sample is excited with a 532 nm laser, and the laser power was kept low (≤ 0.1 mW) to avoid local heating. The spectra were collected using an Andor spectrometer equipped with 2400 grooves per mm grating coupled with an Andor CCD detector, providing a resolution of approximately 1 cm^{-1} . Temperature-dependent measurements were performed with a continuous closed-cycle He-flow cryostat (Montana Instruments). Angle-resolved Raman measurements at MIT were performed using Horiba LabRAM HR Evolution, while those at BC employed a custom-built low-temperature Raman setup⁵⁹. The incident and scattered light polarization were controlled using half-wave plates with a fixed

analyzer while keeping the sample mounted inside the vacuum chamber. The spectra were averaged from three sets of measurements carried out in the same environment to ensure reproducibility. All Raman measurements were carried out on freshly exfoliated flakes.

In-situ cryogenic STEM measurements Single crystal ErTe_3 was exfoliated onto a SiO_2/Si substrate using the Scotch® tape method in an argon-filled glovebox. ErTe_3 flakes of desired thickness (~ 46 nm) were identified using an optical microscope and then transferred to a MEMS-based TEM chip from DENS Solutions using polypropylene carbonate (PPC) polymer. The TEM chip was sealed inside the glove box and then transferred into a portable nitrogen-filled glovebag, inside which the TEM chip was loaded onto a HennyZ cryo-TEM holder capable of continuous temperature control from ~ 100 -1000 K⁶⁰. The holder was loaded in an FEI Titan Themis S/TEM in the nitrogen environment. Thus, the ErTe_3 flakes were never exposed to ambient atmosphere. The LACBED patterns were acquired at 60 kV in the nanoprobe mode, with a convergence angle of 30 mrad. The sample stage was first set to its eucentric height, where a converged beam of electrons is focused on the sample. The stage is then raised by ~ 3 μm above the eucentric height, which results in a small circular area (~ 200 nm) of the ErTe_3 flake to be illuminated by the electron beam, and a spot diffraction pattern is formed in the image plane. Next, we insert a selected-area aperture to block all diffracted beams, allowing only the direct central beam to form a LACBED pattern in the diffraction plane.

RA-SHG measurements RA-SHG measurements were taken under an oblique incidence geometry with an incident angle of $\theta = 11.5^\circ$, incident fundamental wavelength of 800 nm, and reflected SHG wavelength of 400 nm. The laser is operated at a repetition rate of 200 kHz, a pulse duration of 50 fs at the sample site, and a focused beam full-width half maximum (FWHM) of 30 μm on the sample. A typical incident power is 1.0 mW, corresponding to a fluence of 0.7 mJ/cm². RA-SHG records the SHG intensity as a function of an azimuthal angle ϕ between the light scattering plane and the in-plane a -axis, in four polarization channels,

$P_{in}P_{out}$, $S_{in}P_{out}$, $P_{in}S_{out}$, and $S_{in}S_{out}$, where $P/S_{in/out}$ stands for the polarization of the incoming/outgoing (in/out) light being parallel/normal (P/S) to the light scattering plane. The incident and reflected polarizations are defined by a half-wave plate and a linear polarizer, respectively, whereas the reflected SHG wavelength is filtered through two short pass and one bandpass filter with a total optical density (OD) = 18 for the fundamental wavelength. Due to the air sensitivity of LaTe_3 , the samples were mounted into a cryostat inside a 99.999% N_2 -filled glovebox to minimize the air exposure. The RA-SHG measurements were performed under a pressure less than 3×10^{-7} mbar and across a temperature range between 80 K and 270 K.

μ SR measurements The μ SR measurements were carried out at the π M3 beamline using the general purpose surface-muon instrument⁶¹ at the Paul Scherrer Institute, Switzerland. The single-crystalline samples of LaTe_3 were mounted in a ${}^4\text{He}$ gas-flow cryostat. We utilized the spin-rotated mode, where the muon spin is tilted approximately 45° with respect to the beam momentum. The sample is surrounded by three detector pairs: Forward/Backward, Up/Down, and Left/Right. The data presented in this text was from Forward and Backward detectors located along the horizontal beamline. The data were analyzed using the MUSRFIT software package⁶².

Acknowledgement This work was primarily supported by the Air Force Office of Scientific Research under Grants No. FA9550-20-1-0282 (B.S., K.M.K., R.S., Y.W., L.M.S., and K.S.B.), FA9550-20-1-0260 (S.A.A.G., and J.C.) and FA9550-21-1-0423 (R.M.F.). Some Raman experiments were enabled by equipment provided through AFOSR DURIP award FA9550-20-1-0246. Work by GM and MG was supported by the National Science Foundation, Award No. DMR-200334 and DMR-2310895. PS and VMP are grateful for the support of the US Department of Energy (DOE), Office of Science, Office of Basic Energy Sciences under award number DE-SC0018675. The cryogenic STEM and LACBED experiments by SS, SDF and JJC were supported by the US DOE, Basic Energy Sciences program (DE-SC0023905). This work made use of the electron microscopy facility of PARADIM, which is supported by the NSF under Cooperative

Agreement No. DMR-2039380, and CCMR Shared Facilities which are supported through the NSF MRSEC program (DMR-1719875). The FEI Titan Themis 300 was acquired through NSF-MRI-1429155, with additional support from Cornell University, the Weill Institute, and the Kavli Institute at Cornell. WZ and LZ acknowledges the support by the National Science Foundation through the Materials Research Science and Engineering Center at the University of Michigan, Award No. DMR-2309029. XL acknowledges the support by the AFOSR YIP grant no. FA9550-21-1-006. JC is partially supported by the Alfred P. Sloan Foundation through a Sloan Research Fellowship and the Flatiron Institute, a division of the Simons Foundation. The muon work is based in part on experiments performed at the Swiss Muon Source S μ S, Paul Scherrer Institute, Villigen, Switzerland.

Author contributions BS performed the Raman experiments and analyzed the data. GM and KMK helped with data collection. RS and LMS grew the crystals. VMP and YW assisted in the setup of the automated low-temperature microscope. MG helped with sample preparation for Raman measurement. CAO and RC helped in Raman measurement. SS, SDF and JJC performed *in-situ* cryogenic STEM measurements, WZ, XL, and LZ performed SHG measurements, PS, BS, TJH, CB, HL, and MJG performed the muon spin relaxation measurements. EMK helped in muon spin relaxation data analysis. SA, SAAG, JC, and RMF developed the theory. BS wrote the manuscript with the help of KSB. KSB and LMS conceived and supervised the project. All authors contributed to the discussion of the manuscript.

Competing interests The authors declare no competing interests.

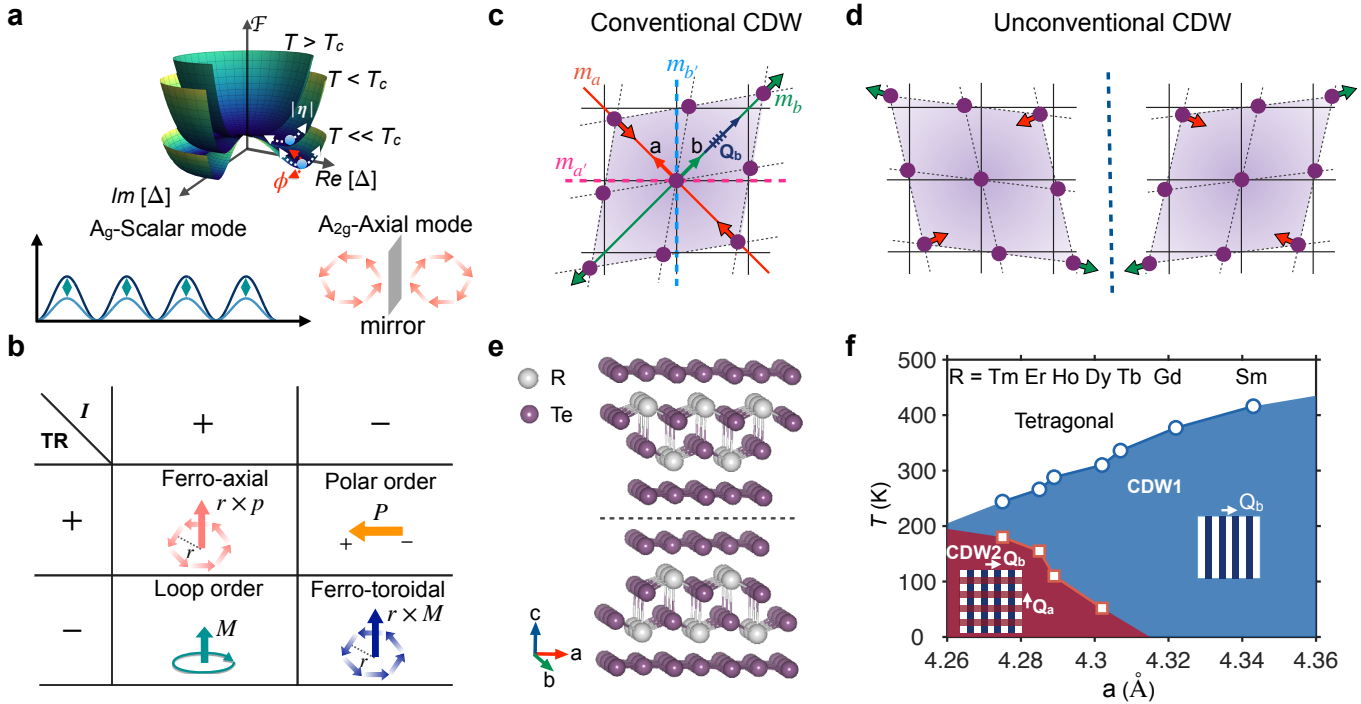


Fig. 1: Spontaneous symmetry breaking. **a** Free energy versus CDW order parameter components (top), and a diagram of the conventional (A_g -scalar) and unconventional (A_{2g} -axial) CDW amplitude modes (bottom).

b The ferroic order parameters possible under inversion (I) and time-reversal (TR)^{24,63}. **c** Schematic for the conventional unidirectional CDW distortion, breaking translation, C_4 -rotation, and diagonal mirrors ($m_{a'}$ (pink) and $m_{b'}$ (blue)) symmetries. Solid line represents unbroken vertical mirrors (m_a (red) and m_b (green)) plane, and dark blue arrow along b -axis represents CDW wave-vector (Q_b). Purple circle indicates the Te-atoms. **d** Unconventional (ferroaxial) CDW order breaking translation, rotation, and all vertical (m_a , m_b) and diagonal ($m_{a'}$, $m_{b'}$) mirror symmetries. **e** Crystal structure of RTe₃ (dashed line indicates the glide plane). **f** Phase diagram of RTe₃ as a function of lattice parameter. Inset shows the unidirectional (dark blue) and bidirectional (red) CDW states.

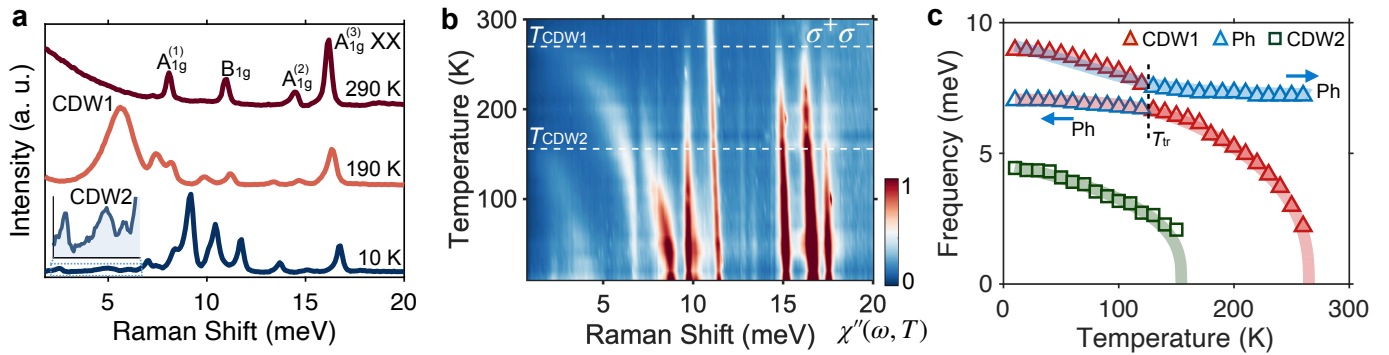


Fig. 2: Temperature-dependent Raman response of ErTe₃. **a** Raman spectra of ErTe₃ at 290 K, 190 K, and 10 K in parallel (XX) polarization configuration (the superscript in the mode symmetry at 290 K is used to distinguish three A_{1g} modes). Inset shows the CDW2 AM (amplitude mode) and folded-phonons at 10 K. **b** Temperature-dependent Raman color map in the crossed-circular ($\sigma^+\sigma^-$) polarization configuration. The dashed white line indicates the CDW transition temperatures. **c** Ginzburg-Landau model fitting of the CDW2 amplitude mode as well as the coupled CDW1 amplitude mode and corresponding folded phonon mode. The solid red, blue, and green lines are fitted curves.

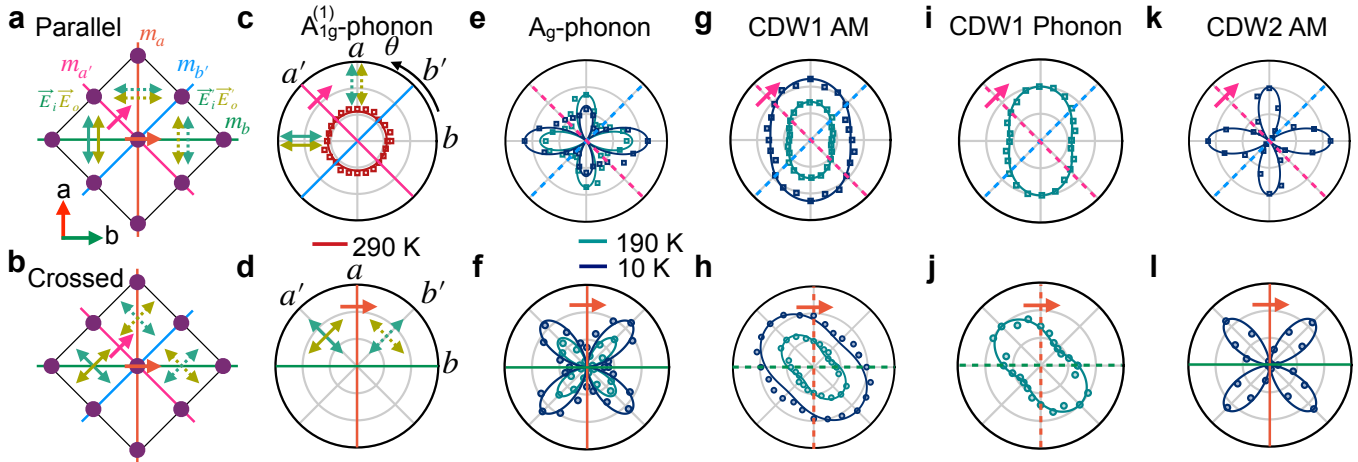


Fig. 3: Angular dependence of the phonon modes and CDW AM (amplitude mode) intensity in the parallel (XX)-(top) and crossed (XY)-(bottom) polarization configurations. a,b Schematic illustrating the response of the mirrors in the parallel (a) and crossed (b) polarization configurations. Solid green and dark yellow arrows represent incident (\vec{E}_i) and outgoing (\vec{E}_o) polarization vectors, and dashed green and dark yellow arrows are the corresponding incident (\vec{E}'_i) and outgoing (\vec{E}'_o) polarization vectors under mirror transformation. **c,d** Angular response of the intensity of $A_{1g}^{(1)}$ (8.1 meV) phonon modes in XX (c), and XY (not observed) (d) at 290 K (undistorted phase). **e,f** Angular response of the intensity of A_g (11.3 meV) phonon modes in XX (e), and XY (f), in the two CDW states at 190 K and 10 K (distorted phase). The response is consistent with the transition to an orthorhombic state with only breaking m'_a and m'_b mirrors. **g,h** CDW1 AM in XX (g) and XY (h), at 190 K and 10 K, **i,j** CDW1 phonon (7.5 meV) in XX (i) and XY (j), at 190 K (display two-fold behavior consistent with the axial response, where all the vertical (m_a, m_b) and diagonal (m'_a, m'_b) mirrors are broken). **(k,l)** CDW2 AM in XX (k) and XY (l) at 10 K respecting m_a and m_b mirrors consistent with A_g symmetry. Solid curves are fitted with angular-dependence mode intensity equations as described in Table 1 of the Supplementary Section 2.

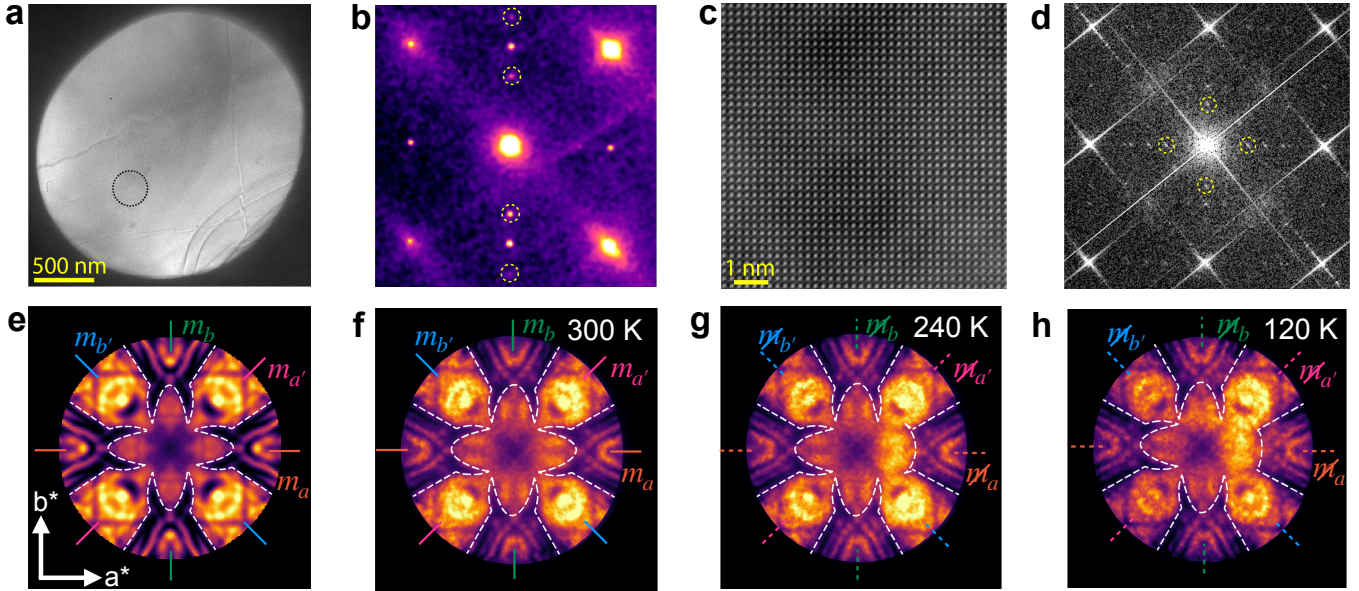


Fig. 4: Large-angle convergent beam electron diffraction (LACBED) on ErTe_3 . **a** Bright-field TEM image of an ErTe_3 flake. The black circle highlights the region from where the LACBED patterns were acquired. **b** SAED pattern taken on flake (a) at 240 K showing the satellite peaks (dotted yellow circles) from the high-temperature CDW1 phase. **c** Atomic-resolution HAADF-STEM image of ErTe_3 taken at 120 K (bidirectional CDW state) in the [001] zone axis. **d** Fast Fourier transform of the atomic-resolution image (c), dotted yellow circles indicate the satellite peaks from the two CDWs at 120 K. **e** Simulated LACBED pattern for a ~ 46 nm thick ErTe_3 flake without any broken symmetries, with the symmetric features highlighted by the overlaid dashed white lines. **f-h** Experimental LACBED patterns of ErTe_3 flake at 300 K (f), 240 K (g), and 120 K (h). Notice the changes in the dark features at the right half of the LACBED patterns below CDW1 transition temperature (indicated by dashed lines), reflecting the broken vertical (m_a, m_b) and diagonal ($m_{a'}, m_{b'}$) mirrors symmetries.

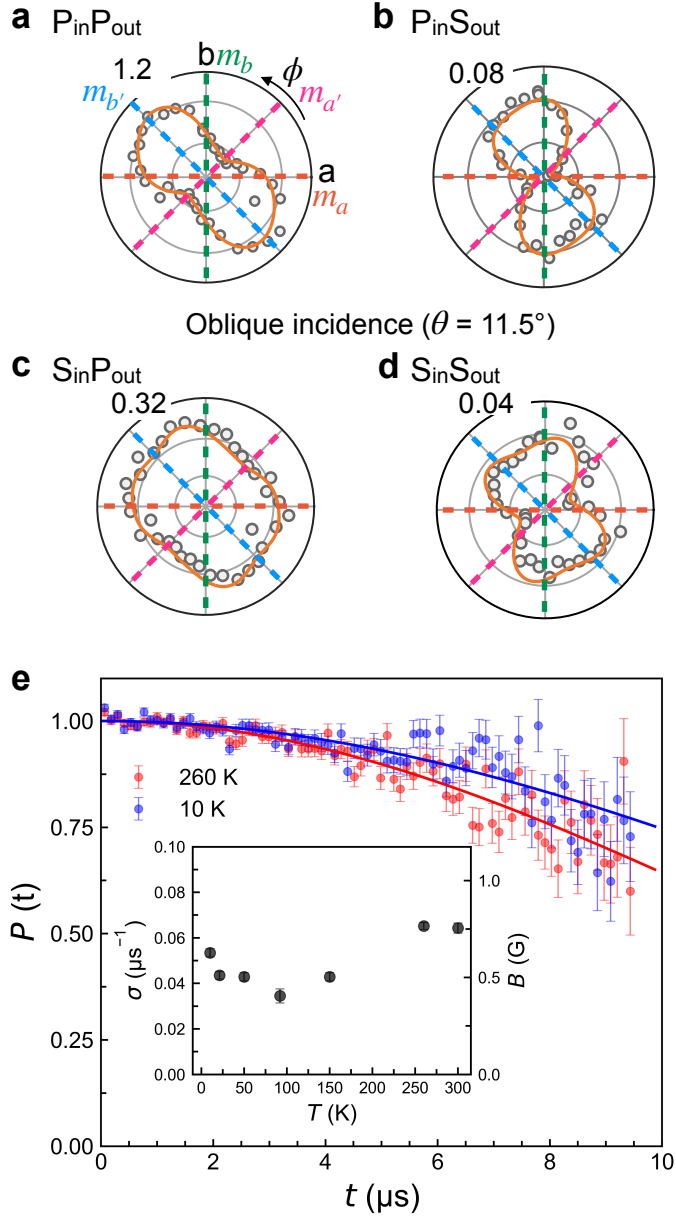


Fig. 5: Broken symmetries in RA-SHG and μ SR data of LaTe_3 . **a-d** Polar plots of RA-SHG data in four polarization channels, $P_{in}P_{out}$ (**a**), $P_{in}S_{out}$ (**b**), $S_{in}P_{out}$ (**c**), and $S_{in}S_{out}$ (**d**) taken at 80 K on LaTe_3 . Circles and solid lines denote the raw data and the fitting to the EQ RA-SHG under the C_{2h} point group, respectively. The dashed lines in every plot indicate the original vertical and diagonal mirror planes. **e**, The ZF- μ SR time spectra for LaTe_3 obtained at 260 K (10 K) represented by solid red (blue) circles. The solid lines are the fittings of the data using the Gaussian Kubo-Toyabe function⁵¹. The inset shows the temperature dependence of the extracted relaxation rate, σ and the equivalent width of the B -field on the right y -axis. The value is consistent with the La nuclear moment, reflecting no TRSB.